Check for updates

First-principles simulation of an ejected electron produced by monochromatic deposition energy to water at the femtosecond order

Takeshi Kai, [ID] *[a] Tomohiro Toigawa, [ID] [a] Yusuke Matsuya, [ID] [ab] Yuho Hirata, [ID] [a] Tomoya Tezuka,[c] Hidetsugu Tsuchida [ID] [cd] and Akinari Yokoya [ID] [e]

This study uses a time-dependent first-principles simulation code to investigate the transient dynamics of an ejected electron produced in the monochromatic deposition energy from 11 to 19 eV in water. The energy deposition forms a three-body single spur comprising a hydroxyl radical (OH$^{\bullet}$), hydronium ion (H_3O^+), and hydrated electron (e_{aq}^-). The earliest formation involves electron thermalization and delocalization dominated by the molecular excitation of water. Our simulation results show that the transient electron dynamics primarily depends on the amount of deposition energy to water; the thermalization time varies from 200 to 500 fs, and the delocalization varies from 3 to 10 nm in this energy range. These features are crucial for determining the earliest single-spur formation and facilitating a sequential simulation from an energy deposition to a chemical reaction in water photolysis or radiolysis. The spur radius obtained from the simulation correlates reasonably with the experimental-based estimations. Our results should provide universalistic insights for analysing ultrafast phenomena dominated by the molecular excitation of water in the femtosecond order.

Introduction

Water photolysis and radiolysis are attractive research fields because of their importance in nuclear reactors, transuranic and high-level mixed waste storage, industrial applications, radiation biology, and medicine.[1,2] Water radiolysis[3–8] or photolysis[9–21] produces various reactive products, such as hydroxyl radicals (OH$^{\bullet}$), hydronium ion (H_3O^+), and hydrated electrons (e_{aq}^-) *etc.*, and their thermal diffusions proceed chemical reactions. When monochromatic short-pulse lasers are irradiated into water, extremely low-energy electrons are ejected by photolysis.[9–21] Consequently, a three-body single spur comprising OH$^{\bullet}$, H_3O^+, and e_{aq}^- is formed. Furthermore, the radiolysis forms a single spur when the deposition energy is <19 eV because the lowest electronic excitation and ionization energies are 8.4 eV and 10.9 eV, respectively.[22,23] Previous photolysis experiments at ∼8 eV energy deposition revealed that the ejected electrons, *i.e.*, the prehydrated electrons (e_{pre}^-), are

weakly trapped in the bulk water at ∼100 fs.[9–13] The e_{pre}^- transitions to e_{aq}^- by the orientation polarization after several 100 fs.[9–13] However, no method has been proposed to directly measure the initial spatial distribution of e_{aq}^-, with a mean distance of a spur radius.

Three processes classify these radiation-induced phenomena. Ultrafast phenomena, such as radiation transport, energy deposition, and electron ejection, are categorized in the physical process (a few fs). The physicochemical process corresponds to the deceleration, thermalization, delocalization (within a few 100 fs), and hydration (within a few 10 ps) of the ejected electrons. Delocalization indicates the spatial distribution of a few nm of the electrons ejected from the parent cations; the initial chemical species are typically determined in this process. The diffusion and reaction of the chemical species are categorized in the chemical process (after a few 100 ps). In the physical process, the incident and ejected electron trajectories are calculated using Monte Carlo codes (MCCs),[2,24–33] such as the Kyushu University Radiobiology Unit Code (KUR-BUC),[2,27,28] the TRACk structure of Electrons in Liquid water (TRACEL),[25] TRACELE,[26] RITRACKS,[29] PARTRAC,[30] Geant4-DNA,[31] and Particle and Heavy Ion Transport code System (PHITS).[32,33] Although Geant4-DNA enabled the electron deceleration calculation down to eV in the latest developments,[34–36] MCCs typically need cutoff energy for electron deceleration (7–10 eV).[34] Molecular excitations are crucial when the electron deceleration is <7 eV, such as intramolecular and intermolecular vibrations and rotation induced by the low-energy electrons

[a]Nuclear Science and Engineering Center, Japan Atomic Energy Agency, 2-4 Shirane Shirakata, Tokai-mura, Naka-gun, Ibaraki, 319-1195, Japan

[b]Faculty of Health Sciences, Hokkaido University, Kita-12 Nishi-5, Kita-ku, Sapporo, Hokkaido 060-0812, Japan

[c]Department of Nuclear Engineering, Kyoto University, Nishikyo-ku, Kyoto 615-8530, Japan

[d]Quantum Science and Engineering Center, Kyoto University, Gokasho, Uji, Kyoto 611-0011, Japan

[e]Institute for Quantum Life Science, National Institutes for Quantum Science and Technology, 4-9-1 Anagawa, Inage-ku, Chiba-shi 263-8555, Japan

in liquid water. However, the cross-sections of liquid water still need to be determined. When analysing the physicochemical process in water radiolysis based on simulation,[2,24–36] the initial spatial distribution of e_{aq}^- must be modelled based on experimental evidence.[34,37,38] For water photolysis,[14–21] the distributions have been reversely predicted from the chemical process calculations for reproducing experimental results (experimental prediction). Therefore, the earliest formation process of a single spur has been unclear.

We developed a dynamic MCC for the physical process (dmcc_phys) to investigate ejected electron thermalization, delocalization, and relocalization in water.[39–46] The code simulates physical and physicochemical processes by implementing cross-sections from 1 meV to 1 MeV.[45,46] Implementing the molecular excitation cross-sections of liquid water[40] allows for a detailed analysis of the physical and physicochemical processes.[45,46] Thus, our simulation provides a clue to unravel the unclear earliest single-spur formation. We used the dmcc_phys to investigate the physicochemical nature of ejected electrons produced by water photolysis at 12.4 eV.[46] Our results for electron delocalization correlated well with the experimental predictions,[19] and some electrons relocalized into parent cations. In other words, the results[46] will reproduce successive chemical reactions in water photolysis experiments.[19] By connecting our code to the chemical codes,[47–50] we should provide a sequential simulation from an energy deposition to a chemical reaction in the three-body single spur without physicochemical models.[34,37,38]

Several models for low-energy electron range calculations below a few eV have been devised from these backgrounds.[34,37,38] However, those models assumed that water irradiates the incident electrons; therefore, they cannot predict the spatial distribution of the electron ejected from the parent cation. This study considered that an incident electron motion was not simulated but only ejected electron motion. Fig. 1 shows the difference between the conventional approach and our approach. A minor spur radius calculation involved in the ejected electron has been reported.[43,46] Moreover, it is impossible to measure the spur radius directly; therefore, the time-evolution yields of e_{aq}^- are measured under irradiation conditions where the simplest radiolytic unit, a three-body single spur, is formed.[14–19] Using a chemical code,[14–19] a parameter analysis is performed to evaluate the initial spur radius that reproduces these experimental results.[14–19] In this analysis, the only spur radius is an unknown free parameter, so its value strongly reflects the experimental results; therefore, this study calls these values experimental predictions. The experimental predictions are reported from 8 eV to 12.4 eV,[14–19] but there are two ionization mechanisms. Ionization from 8 eV to 10.9 eV (ionization energy[23]) deposition energy occurs due to proton-coupled electron transfer,[19] and the deposition energy above the ionization energy produces typical ionization.

This study investigates the ejected electron thermalization, delocalization, and relocalization dominated by the coulombic force of parent cation and the molecular excitation of liquid water at a deposition energy of 11–19 eV to unravel the unclear earliest single-spur formation because our code cannot accurately simulate proton-coupled electron transfer. First, we present the simulation results of the mean ejection distance and kinetic energy of the ejected electrons. Then, we present the simulation results of the kinetic energy and spatial distributions of the ejected electrons. Finally, we evaluate the spur radius and thermalization time at 11–19 eV and compare our evaluation with the experimental predictions and value at 8–12.4 eV.[14–21] Therefore, the experimental prediction values in the 11–12.4 eV energy range are helpful for our code validation. We successfully performed an experimental analysis of the photolysis for a deposition energy of 12.4 eV.[46] For water radiolysis, various energies are deposited into the water. Our results contribute to a much deeper understanding of the earliest formation process of a three-body single spur formed by water radiolysis.

Methods

The dmcc_phys uses time-dependent first-principles simulation to simulate electron deceleration, thermalization, delocalization, and relocalization in the physicochemical process.[39–46] Our code does not require a cutoff energy; a cutoff time is necessary. In the simulation, the dynamical motions of the ejected
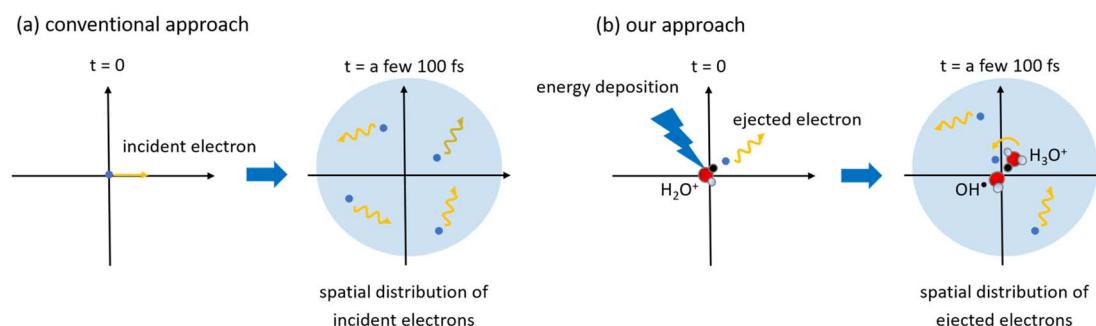

Fig. 1 An illustration of the (a) conventional approach and (b) our approach in simulation studies of low-energy electrons. Conventional approaches report several models for the range calculations of low-energy electrons irradiated into water as a function of incident electron energy.[34,37,38] In our approach,[43,46] we calculated the spatial distribution of ejected electrons generated in water using a first principles simulation. As our code considers the coulombic field of a parent cation, the delocalization and relocalization of ejected electrons can be calculated. When the ejected electrons slow down sufficiently, they hydrate, and a three-body single spur comprising OH·, H_3O^+, and e_{aq}^- is formed.

electrons are calculated using the molecular dynamics (MD) and the time-dependent Monte Carlo (MC) methods.[45,46] Our code was developed by implementing MD based on a Newtonian equation into the time-dependent MCC based on the probability theory of collision.[45,46] PHITS is a general-purpose MCC that can analyse the radiation kinetics at microscopic and macroscopic scales.[32,33] Conversely, the electron track structure mode of PHITS,[32,33] corresponding to the MCC, was previously developed by eliminating MD and replacing the time-dependent MC with the time-independent MC in our code.[32,33] The dmcc_phys simulates the electron dynamic motion in the coulombic field created by the parent cation.[45,46] This coulombic field is shielded along the dielectric response, which is the time evolution of the relative dielectric constant.[45,46] The dielectric response simplifies the hydration process.[45,46] Our code considers the dielectric response comprising electronic, phonon, and orientation polarizations. Thus, the electron or cation charges in water are gradually shielded.[46] Our code could distinguish between the free electrons, e_{pre}^-, and e_{aq}^- *via* the dielectric response.[46] We indicated that the phonon and orientation polarizations contribute to the e_{pre}^- and e_{aq}^- formation, respectively.[46] Our code does not consider electron mass change *via* the dielectric response.[46] However, this assumption is acceptable to calculate the electron dynamics after a few 100 fs because the electrons are nearly stopped at the phonon (prehydration) and orientation (hydration) polarization timescales.[46] Our previous reports showed a detailed flowchart of our water radiolysis and photolysis code,[45,46] clarifying the difference between our code[39–46] and the MCCs.[2,24–36] Furthermore, we show the flowchart of typical MCCs and dmcc_phys to explain those differences in Fig. 2. The subsections describe the

cross-sections, time-dependent MC and MD methods, and spur radius.

Cross-sections

The database of the electron collision cross-sections used herein (Fig. 3) is shown in our previous studies,[45,46] and the database was implemented into PHITS.[32,33] The molecular excitation cross-sections of water differ substantially between the gas and condensed phases. The electron impact cross-sections for elastic scattering, intramolecular and intermolecular vibrations, and rotation excitations are essential to analyse the ejected electron motion. Fig. 3(a) shows the rotation excitation cross-sections;[40] for comparison, the rotation excitation cross-section for water vapor[51] is also shown. Fig. 3(b) shows the intermolecular vibration excitation cross-sections. In our previous study,[40] the data were calculated by an optical approximation using the complex dielectric function of liquid water. However, since the approximation cannot reproduce the resonance structure, the data above 1.7 eV were connected by scaling the amorphous ice data to our data. Fig. 3(c) shows the intramolecular vibrational excitation cross-sections. We used the amorphous ice data to obtain the cross-sections for the condensed phase.[52] The data were connected by scaling the water vapor data[52] to the amorphous ice data because no data below 1.7 eV has been reported. Fig. 3(d) shows our total molecular excitation cross-sections. For comparison, the cross-sections of rotation excitation for the water vapor,[51] total intramolecular vibration excitation for the water vapor,[51] and total intermolecular vibration excitation for the amorphous ice[52] are shown. In doing so, we excluded water vapor information in developing our cross-section database.
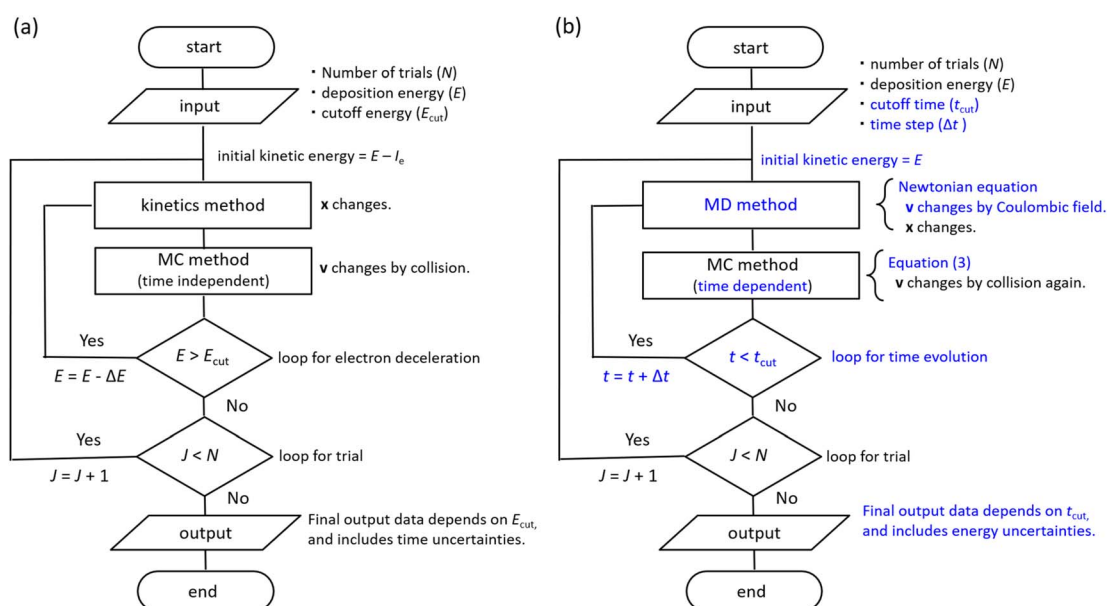
Fig. 2 (a) Flowchart of typical Monte Carlo codes (MCCs) for simulating an ejected electron generated by water photolysis or radiolysis, where I_e is the ionization energy (10.9 eV), ΔE is the energy loss, **x** is the position vector, and **v** is the velocity vector, which is only determined by MC method. (b) Flowchart of dmcc_phys for simulating a ejected electron generated by water photolysis or radiolysis. Here, the initial kinetic energy of an ejected electron equals the deposition energy E. MC and MD methods determine the velocity vector. The molecular dynamics method allows electron relocalization.

A previous study[53] measured dissociative electron attachment (DEA) in low-energy electron irradiation experiments using amorphous water films. In 2000, DNA double-strand breaks triggered by the DEA were measured using DNA films in a vacuum in low-energy electron irradiation experiments.[54] DNA damage yields were also quantified in low-energy electron irradiation below 30 eV using hydrated plasmid DNA films.[55] From the experimental evidence, the DEA attracted attention as a new elementary DNA damage process; however, the DEA was hardly induced in aqueous solution.[56] Geant4-DNA sets the initial G-value of the DEA at 0.02 1/(100 eV) in liquid water.[57] The G-value is reasonable because it well reproduces the experimental results of subsequent chemical reactions.[57] From the background, DEA induction yields seem to strongly depend on the experimental conditions. Since we are targeting liquid water, this study did not consider the DEA cross-section, but further discussion might be needed.

Moliere's elastic scattering cross-section was used,[58] which is much higher than the molecular excitation cross-sections.[45,46] Therefore, we assumed that the scattering angle of electrons changes in inducing the elastic scattering in this study. The scattering angle was sampled from the differential cross-section of the elastic scattering.[58]

When elastic scattering is induced, no energy change occurs in the relative motions of an electron and a water molecule; however, the energy for the motion of the centre-of-mass system changes.[54,55] This phenomenon is evaluated using the momentum transfer cross-section σ_{mom} obtained from the differential cross-section $q(\vartheta)$ of elastic scattering.[59,60]

$$\sigma_{mom} = 2\int_0^\pi (1 - \cos\vartheta)q(\vartheta)\sin\vartheta\, d\vartheta \qquad (1)$$

Using the σ_{mom} of eqn (1) and integral cross-section of elastic-scattering σ_{elas}, the energy transfer is given as[45,46,59,60]

$$\Delta E \cong \frac{2m}{M}\frac{\sigma_{mom}}{\sigma_{Elas}}(E_e - E_{mol}) \qquad (2)$$

where m and M are the mass and E_e and E_{mol} are the kinetic energies of the electrons and water molecules, respectively. E_{mol} was sampled from the Maxwellian of 300 K bulk water. When $E_e > E_{mol}$, the electrons provided a little energy to the water, whereas when $E_e < E_{mol}$, the electrons received a little energy from the water. Although ΔE is approximately a few μeV, the electron kinetic energy distribution approaches the Maxwellian of 300 K bulk water according to eqn (2).[45,46]

Time-dependent MC and MD method

The general MCCs provide the one-step distance of an electron moving to the next collisional position in the water as $\Delta s = -\lambda \ln(k)$,[25] where λ is the mean free path and is obtained from the total cross-section σ and atomic density N (3.318565×10^{22} molecules per cm³) as $\lambda = 1/(\sigma N)$; k is a uniform random number. This code assumes that collisions between electrons and water are induced if the following conditions are satisfied,[45,46]

$$1 - \exp\left(-\frac{\Delta s}{\lambda}\right) > k, \qquad (3)$$

where $\Delta s = v\Delta t$, where v is the absolute value of the velocity of an electron, and Δt is the time step set to 1 attosecond. After determining the collided position of an electron, the collision process is identified and sampled from the ratio of each cross-section. The inelastic-scattering cross-sections (of rotation and intermolecular and intramolecular vibrations) are close to zero
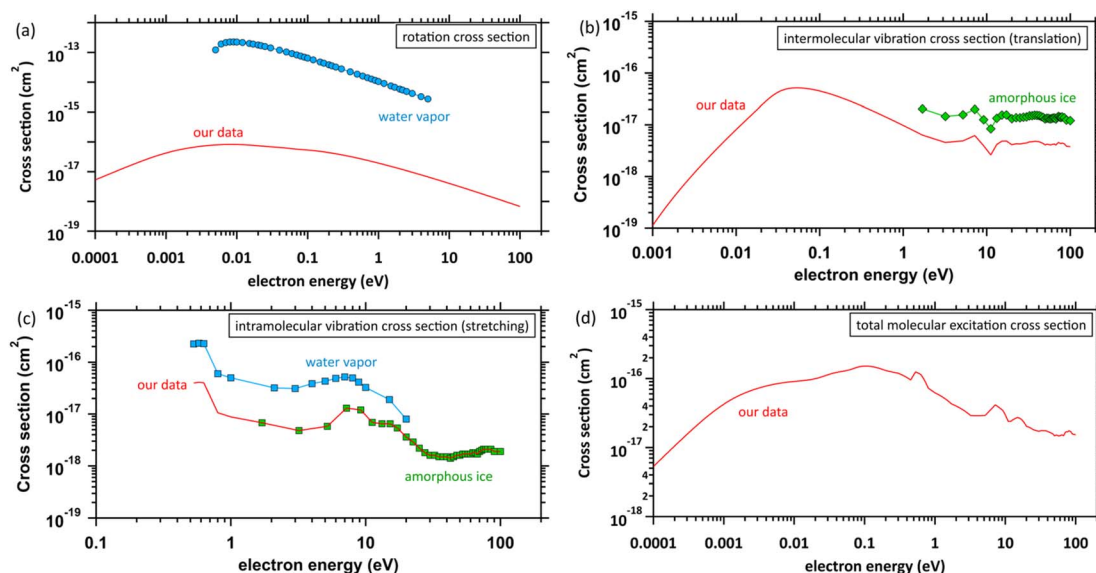

Fig. 3 Molecular excitation cross-sections: (a) rotation excitation cross-sections, red solid line: our data (liquid water), ○: other data (water vapor),[51] (b) intermolecular vibration excitation cross-sections, red solid line: our data (liquid water), ◇: other data (amorphous ice),[52] (c) intramolecular vibration excitation cross-sections, red solid line: our data (amorphous ice base), □: other data (water vapor),[51] ◇: other data (amorphous ice),[52] and (d) total molecular excitation cross-section, red solid line: our data.

with the decreasing electron energy. However, the elastic scattering cross-section has a large finite value.[45,46] Thus, the mean free paths λ of extremely low-energy electrons show very short ranges.

We assumed that the electrons and cations are finite-size particles, a sphere of radius with negative and positive charges (e) uniformly distributed within the sphere (the finite-size particle model).[45,46] The particle radius is 0.099 nm to reproduce the ionization energy of 10.9 eV (ref. 23) and a minimum position of the potential energy (-10.9 eV) is allocated at the origin. When the potential of the cation is expressed in the spherical coordinates, it can be presented in eqn (4).

$$\Phi(r) = \frac{1}{4\pi\varepsilon} \int_{-\infty}^{\infty} \frac{e}{|r - r'|} \mathrm{d}r'$$
$$= \frac{e}{4\pi\varepsilon r}(r \geq a) \ \text{ or } \ \frac{e(3a^2 - r^2)}{8\pi\varepsilon a^3}(r < a), \qquad (4)$$

where e is the elementary charge, ε is $\varepsilon_0 \times \varepsilon_r(t)$. ε_0 is the dielectric constant of the vacuum, and $\varepsilon_r(t)$ is the dielectric response of water,[45,46] causing the potential energy to change with time evolution.[45,46] In the previous MCCs,[2–36] the kinetic energy of the ejected electron is given by subtracting the ionization energy from the deposition energy. However, in our code, an electron with kinetic energy corresponding to the deposition energy (11–19 eV) is ejected from a minimum potential position (origin). A Newtonian equation can solve the dynamic behaviour in the electron–water collision of an ejected electron around a parent cation in water.[45,46] The MC method is a probabilistic method. Therefore, a small number of MC calculation trials results in statistical errors. Our simulations were performed based on the uniform random numbers in the MC method for the collision, and the number of calculation trials was adapted to reach a statistical uncertainty of much less than 1%. The number of histories used for the simulation is 4 million.

Spur radius

We present the numerical data for electron delocalization, *i.e.*, electron number distribution as a function of radius r in polar coordinates. The r is the distance from the ionic core of the parent cation. The numerical data cannot be reproduced with Gaussian or exponential distributions alone because the ejected electron motion depends on the coulombic field of the parent cation and thermal diffusion in water. Thus, we expect the numerical distribution to be reproduced by Gaussian and exponential distributions, especially in the deposition energy around the ionization energy (10.9 eV (ref. 23)). Therefore, the following equation, which multiplies the volume elements by Gaussian $f_{\text{gauss}}(r)$ and exponential $f_{\text{exp}}(r)$ distributions, is used to express the electron delocalization distribution $f(r)$ analytically.

$$f(r) = (Af_{\text{gauss}}(r) + Bf_{\text{exp}}(r))/C \qquad (5)$$

where

$$f_{\text{gauss}}(r) = 4\pi r^2 \left(\frac{2}{\pi\langle r_0\rangle}\right)^3 \exp\left(-\frac{4|r|^2}{\pi\langle r_0\rangle^2}\right)\mathrm{d}r$$

and

$$f_{\text{exp}}(r) = 4\pi r^2 \frac{27}{8\pi\langle r_1\rangle^3} \exp\left(-\frac{3|r|}{\langle r\rangle_1}\right)\mathrm{d}r$$

where r is the distance from the ionic core of the parent cation, and $\langle r_0\rangle$ (or $\langle r_1\rangle$) is the mean distance of the spatial distribution of an electron. H_3O^+ and $OH^{\cdot}$ are near the origin. The spur radius was defined by $A\langle r_0\rangle + B\langle r_1\rangle$. The electron relocalization into the parent cation can be calculated using our code.[43–46] However, the functional distribution fitting for the relocalized electrons was challenging; therefore, it was performed to reproduce the distribution more than 1 nm from the origin. When the numerical distribution is integrated over the entire space, it is normalized to 1 but not when integrated over the region above 1 nm, excluding the relocalized electrons. Therefore, a scaling parameter is necessary to reproduce the region above 1 nm by functional fitting. We introduced the parameter C in eqn (4), which corresponds approximately to electron relocalization yield.

Results and discussion

First, the electrons' mean ejection distance and kinetic energy were presented to determine the cutoff time. The kinetic energy distributions of an electron are presented and compared to the Maxwellian of 300 K bulk water to discuss electron thermalization. The spatial distributions of the ejected electron are presented to evaluate the spur radius. From these results, the thermalization and hydration of electrons produced by water photolysis and radiolysis were finally discussed.

Mean ejection distance and kinetic energy

Fig. 4(a) shows the simulation results with the time evolution of the mean ejection distances, defined as a straight line between the starting point (origin) and the position of the ejected electron at each time. When the deposition energies were 11 and 11.5 eV, the mean ejection distances converged at ~200 fs. When the deposition energies were 12, 13, 14–16, and 17–19 eV, the mean ejection distances converged at 300, 400, and 500 fs, respectively. The e_{pre}^- formation time has yet to be reported as experimental results, except for the 8 eV deposition energy.[9–13] Therefore, defining the cutoff time for all deposition energies is difficult. We defined the cutoff time as the time when the mean energy of the electrons decelerates to roughly a few 100 meV. Then, the mean ejection distances of electrons are well converged. Fig. 4(b) shows the simulation results with time evolution of the mean kinetic energy of the electrons. The cutoff times for each deposition energy were the same as those in Fig. 4(a), and the mean kinetic energy was <1 eV. Previous reports[9–13] measured the e_{pre}^- and e_{aq}^- formations using photolysis experiments at ~8 eV deposition energy, where e_{pre}^- is formed at ~100 fs and e_{aq}^- at several 100 fs. Although these experimental results are yet to be reported in a deposition energy of 11–19 eV, the e_{pre}^- and e_{aq}^- formation time could be longer than the time reported in the photolysis experiments, *i.e.*, around 8 eV.
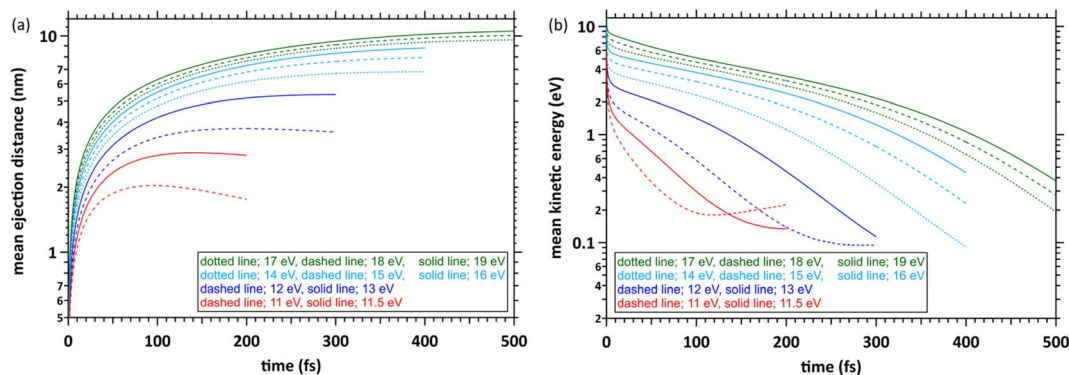
Fig. 4 (a) Mean ejection distance and (b) mean kinetic energy of an electron.
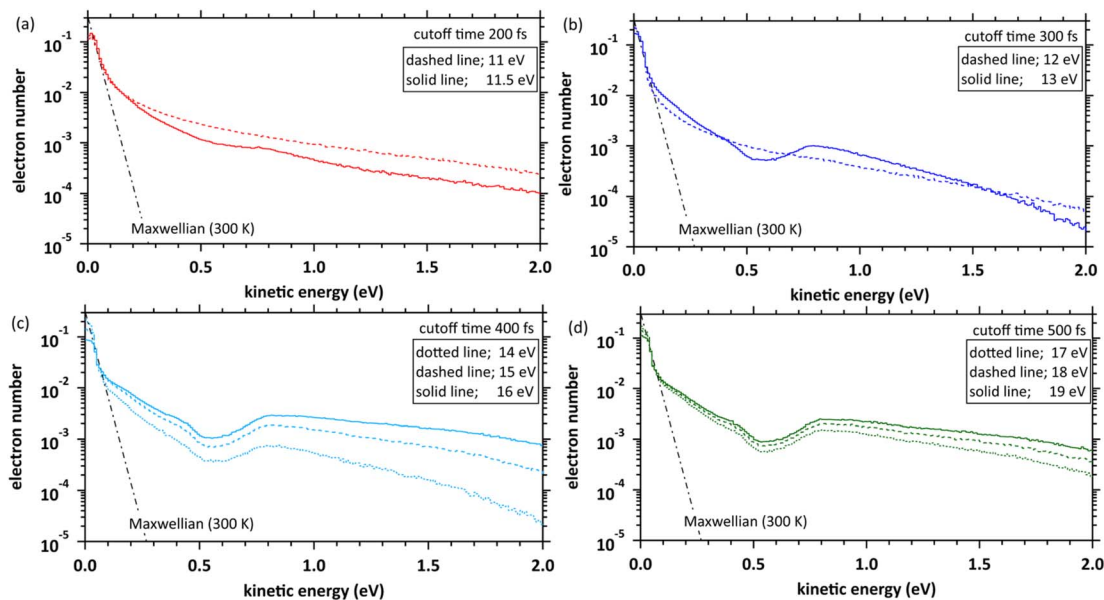

Fig. 5 Kinetic energy distributions of the electron numbers at each cutoff time in the deposition energy region of 11–19 eV. (a) 11 and 11.5 eV, (b) 12 and 13 eV, (c) 14–16 eV, (d) 17–19 eV. The distribution results are spherical coordinates with an energy mesh of $\Delta E = 10$ meV.

Kinetic energy distribution of ejected electrons

Fig. 5 shows our simulation results for the electron kinetic energy distributions at each deposition energy (11–19 eV) and the cutoff times. The molecular excitations, the momentum transfer of eqn (2), and the cation potential of eqn (4) dominate these electron kinetic energy distributions.[46] These results show that the electron kinetic energy distributions exhibit nonthermal equilibrium distributions because some electrons were relocalized into the parent cations due to the coulombic field. In the extremely low-energy region within 0.1 eV, the kinetic energy distribution of electrons, which escaped from the coulombic field, approaches the Maxwellian of 300 K bulk water. Our results indicate that the electrons were sufficiently decelerated at the cutoff time for each deposition energy. Therefore, the cutoff time used herein was reasonable for discussing the spur radius. When the deposition energy exceeded 13 eV, a depression was observed near the kinetic energy distribution of 0.5 eV. A potential reason is the contribution of

intramolecular vibration excitations with resonance structures in the cross-section near several 0.1 eV (see, Fig. 3(c)).

Spatial distribution of ejected electrons

Fig. 6 shows our simulation results of the spatial distributions of the ejected electrons at each deposition energy (11–19 eV) and the cutoff times. The fraction of electrons near the parent cations (within 1 nm) is considerably high at the 11 and 11.5 eV deposition energies near the ionization energy (10.9 eV (ref. 23)). This result indicates that many electrons are relocalized into the parent cations within several 100 fs, even if the deposition energy exceeds the ionization energy. The relocalized electrons will form excited states.[20] The fraction of the relocalized electrons decreases with the increasing deposition energy and becomes negligible at deposition energies above 15 eV. The liquid water has some highly excited states at 11–14 eV.[22] During several 100 fs, many electrons that transited to the Rydberg $(A + B)$ (excitation energy of 11.26 eV (ref. 22)) or
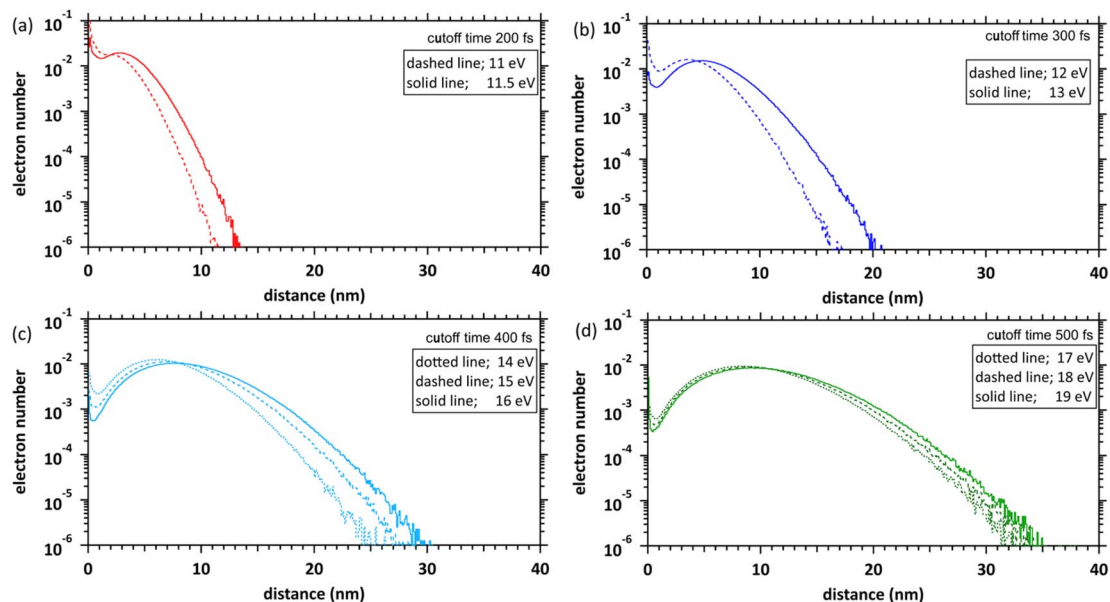
Fig. 6 Delocalization and relocalization distributions of the electron numbers at each cutoff time in the deposition energy region of 11–19 eV. (a) 11 and 11.5 eV, (b) 12 and 13 eV, (c) 14–16 eV, (d) 17–19 eV. The horizontal axis shows the distance from the ionic core to the electrons. The distribution results are spherical coordinates with a spatial mesh of $\Delta r = 0.1$ nm. All solid angle meshes $\Delta\Omega$ in the Δr are integrated.
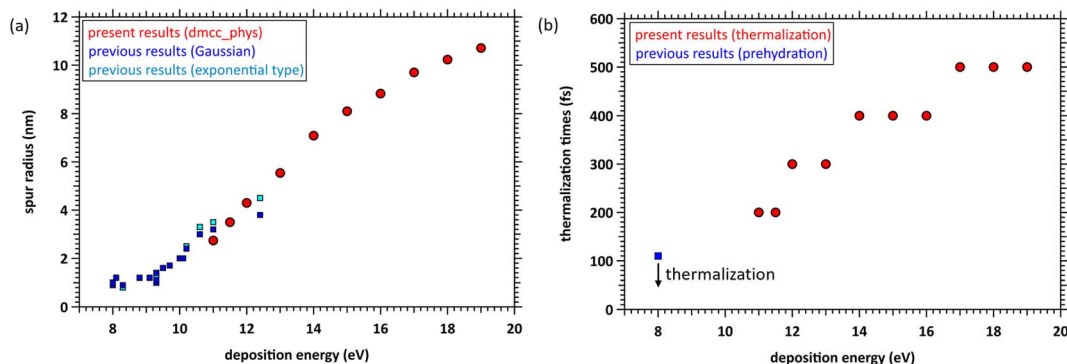

Fig. 7 (a) Spur radii of electrons in the deposition energy region of 8–19 eV; □: experimental predictions,[14–19] ○: present. (b) Thermalization time at the deposition energy region of 11–19 eV, and prehydration times at 8 eV.[10]

Rydberg $(C + D)$ (excitation energy of 11.93 eV (ref. 22)) were finally relocalized. However, the electrons that transited to the diffuse band (excitation energy of 14.1 eV (ref. 22)) were mostly delocalized. These results become a new universalistic insight for analysing the initial yield of e_{aq}^- in water radiolysis.[45] The maxima of these distributions shift from 3 nm to 10 nm as the deposition energy increases.

Spur radius

We determined the spur radius by obtaining the parameters $\langle r_0 \rangle$, $\langle r_1 \rangle$, A, B, and C in eqn (5) by fitting our results (Fig. 6). Fig. 7(a) shows our results (11–19 eV) and previous experimental predictions[14–19] (8–12.4 eV) for the spur radius. The present results, indicated by circles from 11 to 19 eV, reasonably correlate with the previous experimental predictions indicated by squares from 8 to 12.4 eV in Fig. 7(a). Table 1 shows the

fitting parameters ($\langle r_0 \rangle$, $\langle r_1 \rangle$, A, B, and C). From these results, the distributions shift from the exponential type to the Gaussian type as the deposition energy increases. When the deposition energy is <14 eV, Gaussian and exponential distributions are required to reproduce the spatial distribution of the ejected electrons. However, when the deposition energy is >14 eV, it can be approximately represented by a Gaussian. Electron delocalization in the three-body single spur will be easily reproduced using the data listed in Table 1. These distributions correspond to the initial spatial distribution of e_{aq}^-. Although these spur radii were one of the remaining unknown parameters in water photolysis and radiolysis, this study elucidated their values.

Thermalization and hydration

From the photolysis experiments at 8 eV deposition energy,[10] the physicochemical process of water photolysis progresses

Table 1 Parameters of eqn (5) and spur radii at each deposition energy

Energy (eV)	A	r_0 (nm)	B	r_1 (nm)	C	Radius (nm)
11.0	0.2	2.5	0.8	2.8	1.70	2.74
11.5	0.5	3.2	0.5	3.8	1.30	3.50
12.0	0.5	4.4	0.5	4.2	1.20	4.30
13.0	0.8	5.8	0.2	4.5	1.05	5.54
14.0	0.7	6.7	0.3	8.0	1.00	7.09
15.0	0.8	8.0	0.2	8.5	1.00	8.10
16.0	0.9	8.8	0.1	9.0	1.00	8.82
17.0	0.9	9.7	0.1	9.7	1.00	9.70
18.0	0.9	10.2	0.1	10.5	1.00	10.23
19.0	0.9	10.7	0.1	10.8	1.00	10.72

with electron thermalization, prehydration, and hydration. e_{pre}^- was formed at ~110 fs, and e_{pre}^- transitioned to e_{aq}^- at ~240 fs.[10] Although the e_{pre}^- formation time has been reported as experimental results at 8 eV deposition energy,[9–13] proton-coupled electron transfer ionizes the electrons. As our code cannot simulate this mechanism, we show the calculation results for energy deposition above the ionization energy (10.9 eV (ref. 23)). The results in Fig. 4 indicate that the prehydration and hydration times depend on the deposition energy because the thermalization time depends on the deposition energy. Fig. 7(b) shows the thermalization times estimated from the cutoff times herein and the prehydration time reported previously.[10] Our simulation results are discrete (Fig. 7(b) shown in circles), but the linearity is roughly preserved in the energy region from 8 to 19 eV. Therefore, we predict that the prehydration and hydration times will exceed 500 fs, at least when the deposition energy exceeds 17 eV. From the energy-loss function of water reported in our recent literature,[45] a high-energy incident electron in liquid water primarily imparts an energy of ~20 eV to water. Thus, the electron thermalization times differ considerably between water photolysis and radiolysis. Our findings for thermalization and delocalization above 17 eV can provide new universalistic insight into the physicochemical process of water radiolysis. We expect new experimental results with deposition energies above 12.4 eV.

Future

As shown in Fig. 1, previous studies irradiated low-energy electrons into the water, whereas this study analyses the dynamics of ejected electrons resulting from the energy deposited into the water. Consequently, we simulated the delocalization and relocalization of ejected electrons and elucidated the energy deposition dependence of the spur radius and thermalization time. The electrons cannot induce additional ionization or electronic excitation at the deposition energy of 11–19 eV; therefore, a three-body single spur was formed. As the deposition energy increases, the ejected electrons induce additional ionization and electronic excitation, forming multibody single spurs. In a biological system, this spur formation induces complex DNA lesions, such as double-strand breaks, causing biological effects with a certain probability.[61,62] In the future, we will investigate the multibody single-spur formation process in water radiolysis.

Conclusions

We investigated the transient dynamics of an ejected electron produced in the range of monochromatic deposition energy into water using dmcc_phys, resulting in the earliest three-body single spur. We found that electron thermalization, delocalization, and relocalization dominated by the molecular excitation of liquid water in the coulombic field created by the parent cation, largely depend on the amount of deposition energy into the water. In other words, physicochemical timescales differ considerably between water photolysis and radiolysis. The estimated spur radius based on the MD and MC reasonably correlates with the experimental prediction values (8–12.4 eV).[14–19] We validated our simulation code, including the molecular excitation cross-sections of liquid water.

The role of highly excited electrons in water radiolysis is not well understood.[1] Liquid water has some highly excited states at a deposition energy of 11–14 eV.[22] Many electrons that transited to the highly excited states were finally relocalized. However, the ejected electrons were mostly delocalized at the deposition energy of >14 eV. Electron relocalization produces chemical species, such as $OH^\bullet + H^\bullet$ or $O + H_2$, or energy relaxation, originating from electronic excitation, whereas electron delocalization produces chemical species, such as $OH^\bullet$, H_3O^+, and e_{aq}^-, originating from ionization. The scientific insights proposed by this study should be widely available for the subsequent chemical processes in radiation biology,[2] nuclear chemistry,[1] and other fields.

Author contributions

T. Kai and T. Toigawa designed this work. T. Kai developed the dynamic Monte Carlo code for the physical process and performed all calculations. Y. Matsuya and Y. Hirata contributed to the discussion for developing the code and radiation physics. H. Tsuchida and T. Tezuka contributed to the discussion of radiation physics. T. Toigawa contributed to the discussion of radiation chemistry. A. Yokoya supervised this study. T. Kai wrote the manuscript. All authors contributed to the discussion of this study and have reviewed the manuscript.

Conflicts of interest

There are no conflicts to declare.

Acknowledgements

Notes and references

1 B. C. Garrett, et al., *Chem. Rev.*, 2005, **105**, 355–390.

2 H. Nikjoo, D. Emfietzoglou, T. Liamsuwan, R. Taleei, D. Liljequist and S. Uehara, *Rep. Prog. Phys.*, 2016, **79**, 116601.

3 D. M. Bartels, A. R. Cook, M. Mudaliar and C. D. Jonah, *J. Phys. Chem. A*, 2000, **104**, 1686–1691.

4 Y. Muroya, M. Lin, G. Wu, H. Iijima, K. Yoshii, T. Ueda, H. Kudo and Y. Katsumura, *Radiat. Phys. Chem.*, 2005, **72**, 169–172.

5 J. Yang, T. Kondoh, K. Kan and Y. Yoshida, *Nucl. Instrum. Methods Phys. Res., Sect. A*, 2011, **629**, 6–10.

6 G. P. Horne, T. A. Donoclift, H. E. Sims, R. M. Orr and S. M. Pimblott, *J. Phys. Chem. B*, 2016, **120**, 11781–11789.

7 J. Ma, F. Wang, S. A. Denisov, A. Adhikary and M. Mostafavi, *Sci. Adv.*, 2017, **3**, e1701669.

8 K. Kitajima, H. Tsuchida, T. Majima and M. Saito, *J. Chem. Phys.*, 2019, **150**, 095102.

9 A. Migus, Y. Gauduel, J. L. Martin and A. Antonetti, *Phys. Rev. Lett.*, 1987, **58**, 1559–1562.

10 Y. Gauduel, S. Pommeret, A. Migus and A. Antonetti, *J. Phys. Chem.*, 1989, **93**, 3880–3882.

11 C. Silva, P. K. Walhout, K. Yokoyama and P. F. Barbara, *Phys. Rev. Lett.*, 1998, **80**, 1086–1089.

12 M. Assel, R. Laenen and A. Laubereau, *J. Phys. Chem. A*, 1998, **102**, 2256–2262.

13 A. Thaller, R. Laenen and A. Laubereau, *Chem. Phys. Lett.*, 2004, **398**, 459–465.

14 M. U. Sander, M. S. Gudiksen, K. Luther and J. Troe, *Chem. Phys.*, 2000, **258**, 257–265.

15 C. L. Thomsen, D. Madsen, S. R. Keiding, J. Thogersen and O. Christiansen, *J. Chem. Phys.*, 1999, **110**, 3453–3462.

16 D. Madsen, C. L. Thomsen, J. Thogersen and S. R. Keiding, *J. Chem. Phys.*, 2000, **113**, 1126–1134.

17 J. A. Kloepfer, V. H. Vilchiz, V. A. Lenchenkov, A. C. Germaine and S. E. Bradforth, *J. Chem. Phys.*, 2000, **113**, 6288.

18 R. A. Crowell and D. M. Bartels, *J. Phys. Chem.*, 1996, **100**, 17940.

19 C. G. Elles, A. E. Jailaubekov, R. A. Crowell and S. E. Bradforth, *J. Chem. Phys.*, 2006, **125**, 044515.

20 C. G. Elles, I. A. Shkrob, R. A. Crowell and S. E. Bradforth, *J. Chem. Phys.*, 2007, **126**, 164503.

21 J. Savolainen, F. Uhlig, S. Ahmed, P. Hamm and P. Jungwirth, *Nat. Chem.*, 2014, **6**, 697–701.

22 H. G. Paretzke, D. T. Goodhead, I. G. Kaplan, and M. Terrissol, Track structure quantities, in *Atomic and molecular data for radiotherapy and radiation research*, IAEA, Vienna, 1995, ch. 9, (IAEA-TECDOC-799).

23 M. Faubel and B. Steiner, Photoelectron spectroscopy at liquid water surfaces, in *Linking the gaseous and condensed phases of matter. The behavior of slow electrons*, ed. L. G. Christophorou, E. Illenberger and W. F. Schmidt, NATO ASI Series B-326, Plenum Press, New York, 1994, pp. 517–523.

24 S. M. Pimblott and J. A. LaVerne, *J. Phys. Chem. A*, 1997, **101**, 5828–5838.

25 H. Tomita, M. Kai, T. Kusama and A. Ito, *Radiat. Environ. Biophys.*, 1997, **36**, 105–116.

26 V. Cobut, Y. Frongillo, J. P. Patau, T. Goulet, M.-J. Frasher and J.-P. Jay-Gerin, *Radiat. Phys. Chem.*, 1998, **51**, 229–243.

27 H. Nikjoo, S. Uehara, D. Emfietzoglou and F. A. Cucinotta, *Radiat. Meas.*, 2006, **41**, 1052–1074.

28 S. Uehara and H. Nikjoo, *J. Radiat. Res.*, 2006, **47**, 69–81.

29 I. Plante and F. A. Cucinotta, *New J. Phys.*, 2009, **11**, 063047.

30 W. Friedland, M. Dingfelder, P. Kundrát and P. Jacob, *Mutat. Res.*, 2011, **711**, 28.

31 S. Incerti, I. Kyriakou, M. C. Bordage, S. Guatelli, V. Ivanchenko and D. Emfietzoglou, *J. Appl. Phys.*, 2019, **125**, 104301.

32 T. Sato, Y. Iwamoto, S. Hashimoto, T. Ogawa, T. Furuta, S. Abe, T. Kai, P. E. Tsai, N. Matsuda, H. Iwase, N. Shigyo, L. Sihver and K. Niita, *J. Nucl. Sci. Technol.*, 2018, **55**, 684–690.

33 Y. Matsuya, T. Kai, Y. Yoshii, Y. Yachi, S. Naijo, H. Date and T. Sato, *J. Appl. Phys.*, 2019, **126**, 124701.

34 I. Kyriakou, D. Sakata, H. N. Tran, Y. Perrot, W.-G. Shin, N. Lampe, S. Zein, M. C. Bordage, S. Guatelli, C. Villagrasa, D. Emfietzoglou and S. Incert, *Cancers*, 2022, **14**, 35.

35 W.-G. Shin, J. Ramos-Mendez, B. Faddegon, H. N. Tran, C. Villagrasa, Y. Perrot, S. Okada, M. Karamitros, D. Emfietzoglou, I. Kyriakou, M. C. Bordage, D. Sakata, S. Guatelli, H. J. Choi, C. H. Min, S. B. Lee and S. Incerti, *J. Appl. Phys.*, 2019, **126**, 114301.

36 S. Incerti, I. Kyriakou, M. A. Bernal, M. C. Bordage, Z. Francis, S. Guatelli, V. Ivanchenko, M. Karamitros, N. Lampe, S. B. Lee, S. Meylan, C. H. Min, W. G. Shin, P. Nieminen, D. Sakata, N. Tang, C. Villagrasa, H. N. Tran and J. M. C. Brown, *Med. Phys.*, 2018, **45**, e722–e739.

37 S. M. Pimblott and A. Mozumder, *J. Phys. Chem.*, 1991, **95**, 7291–7300.

38 R. H. Ritchie, R. N. Hamm, J. E. Turner, and W. E. Bolch, in *Computational Approaches in Molecular Radiation Biology, Basic Life Sciences*, ed. M. N. Varma and A. Chatterjee, Plenum Press, New York, 1994, vol. 63, pp. 33–44.

39 T. Kai, A. Yokoya, M. Ukai, K. Fujii, M. Higuchi and R. Watanabe, *Radiat. Phys. Chem.*, 2014, **102**, 16–22.

40 T. Kai, A. Yokoya, M. Ukai and R. Watanabe, *Radiat. Phys. Chem.*, 2015, **108**, 13–17.

41 T. Kai, A. Yokoya, M. Ukai, K. Fujii and R. Watanabe, *Radiat. Phys. Chem.*, 2015, **115**, 1–5.

42 T. Kai, A. Yokoya, M. Ukai, K. Fujii and R. Watanabe, *Int. J. Radiat. Biol.*, 2016, **92**, 654–659.

43 T. Kai, A. Yokoya, M. Ukai, K. Fujii and R. Watanabe, *J. Phys. Chem. A*, 2016, **120**, 8228–8233.

44 T. Kai, A. Yokoya, M. Ukai, K. Fujii, T. Toigawa and R. Watanabe, *Phys. Chem. Chem. Phys.*, 2018, **20**, 2838–2844.

45 T. Kai, T. Toigawa, Y. Matsuya, Y. Hirata, T. Tezuka, H. Tsucida and A. Yokoya, *RSC Adv.*, 2023, **13**, 7076–7086.

46 T. Kai, T. Toigawa, M. Ukai, K. Fujii, R. Watanabe and A. Yokoya, *J. Chem. Phys.*, 2023, **158**, 164103.

47 I. A. Plante, *Phys. Med. Biol.*, 2021, **66**, 03TR02.

48 W. G. Shin, J. Ramos-Mendez, N. H. Tran, S. Okada, Y. Perrotf, C. Villagrasa and S. Incerti, *Phys. Med.*, 2021, **88**, 86–90.

49 P. Clifford, N. J. B. Green, M. J. Oldfield, M. J. Pilling and S. M. Pimblott, *J. Chem. Soc., Faraday Trans. 1*, 1986, **82**, 2673–2689.

50 S. M. Pimblott and J. A. LaVerne, *J. Phys. Chem. A*, 1998, **102**, 2967–2975.

51 Y. Itikawa and N. Mason, *J. Phys. Chem. Ref. Data*, 2005, **34**, 1–22.

52 M. Michaud, A. Wen and L. Sanche, *Radiat. Res.*, 2003, **159**, 3–22.

53 P. Rowntree, L. Parenteau and L. Sanche, *J. Chem. Phys.*, 1991, **94**, 8570–8576.

54 B. Boudaïffa, P. Cloutier, D. Hunting, M. A. Huels and L. Sanche, *Science*, 2000, **287**, 1658–1660.

55 E. Alizadeh, A. G. Sanz, G. García and L. Sanche, *J. Phys. Chem. Lett.*, 2013, **4**, 820–825.

56 C.-R. Wang, J. Nguyen and Q.-B. Lu, *J. Am. Chem. Soc.*, 2009, **131**, 11320–11322.

57 W. G. Shin, J. R. Mendez, N. H. Tran, S. Okada, Y. Perrot, C. Villagrasa and S. Incerti, *Phys. Med.*, 2021, **88**, 86–90.

58 G. Moliere, Theorie der streuung schneller gelandener teilchen II: Mehrfachund ielfachstreuung, *Z. Naturforsch.*, 1948, **3**, 78–97.

59 K. Takayanagi, Introduction to electron-molecule collisions, in *Electron-Molecule Collisions*, ed. I. Shimamura and K. Takayanagi, Plenum Press, New York, 1984, pp. 1–87.

60 I. KrajcarBronić, M. Kimura and M. Inokuti, *J. Chem. Phys.*, 1995, **102**, 6552–6558.

61 D. T. Goodhead, *Int. J. Radiat. Biol.*, 1994, **65**, 7–17.

62 J. F. Ward, *Prog. Nucleic Acid Res. Mol. Biol.*, 1988, **35**, 95–125.